Stability analysis and Impedance-based representation of VSC

Yeonjoong Kim

yeonjoong.kim@tecnico.ulisboa.pt

Instituto Superior Técnico, Universidade de Lisboa, Portugal

December, 2021

Abstract—**As high levels of power electronics are integrated into the power grid, the importance of controlling the small-signal stability of the grid system is becoming more important and complex caused by the widen control frequency range. The main purpose of the thesis is to present the design of the grid-connected voltage source converter (VSC) in *MATLAB/Simulink* and how its operating conditions affect the grid stability and impedance responses. The key result includes the validation of the linearized state-space model (SSM), its response under changes of each parameter, and its impedance representation.**

Keywords — voltage source converter, grid stability analysis, eigenvalue analysis, dq impedance

I. INTRODUCTION

The recent transition of the electrical power system from fossil fuel-base to the integration of variable renewable energy (VRE) such as solar and wind has required an evolution in the power system to support variability and uncertainty. Since most countries have set ambitious goals to scale up renewable energy in their energy mix to meet individual national strategy as well as to comply with the Paris agreement treating climate change.

Full-scale, bidirectional voltage source converter (VSC) has emerged as the key element to penetrate VRE into grid [1],[2] in that they allow the improvement on the generation efficiency of VRE as well as the support for grid health with grid-forming capability. Nowadays, with the help of versatility, VSC is widely applied in microgrid interconnecting not only VRE generations but also energy storage systems (ESS) or backup generation systems, such as pumped-storage or gas turbine, to cover the intermittence and enhance the capacity factor, typically 15% in solar PV and 20 percent in wind, of VRE generation.

However, such an increasing number of utility-scale VRE power plants has brought about new kinds of risk on system stability accompanied by much more complexity of analysis. The reason is that high levels of power electronics have adopted operation frequency ranging widely from a couple of Hz to tens of kHz, which makes complex dynamic behavior. Also, most power electronics manufacturers, who are unwilling to share internal designs of their products to the public, only supply the black-box Electromagnetic Transient (EMT) models, which has clear limits on resolving stability of modern grid [3]. For these reasons, transmission system operators (TSO) and distribution system operators (DSO) have difficulties in system operation, predicting and responding to the system malfunction, possibly leaded to black-out.

The objective of the thesis is to analyze the average model of two-level full-bridge VSC connected to a grid with the consideration of its internal dynamics and impact on the grid, with regard to the stability and the characterization of an impedance-based representation enabling the system analysis even when internal design parameters are unknown.

II. LITERATURE REVIEW

A. State-of-the-art power electronics

The utilization of distributed energy resources (DRE) has given rise to the change of a classical centralized power generation system into a distributed power generation system, accompanied by the need for power converters to effectively integrate a DC system into an AC system. Power electronics, represented by inverters and converters, have successfully realized the integration between the AC and the DC grid no matter the grid size, micro-grid or super-grid.

Each converter topology has clear advantages and disadvantages and there exist some investigations on the hybrid of LCC and VSC systems [4]. However, when it comes to the formation of DC microgrid or the transmission system for offshore wind turbines, VSC has recently been in very preference to LCC due to the following reasons:

- Control of voltage depending on the application where it is connected
- Independent active and reactive power control
- Black-start capability to support grid-forming
- Bidirectional power flow without reversing the polarity
- Reduced size of filters compared to other converter technologies

Depending on the arrangement and the connection point of semiconductors, Multilevel converters can be classified into three types; Neutral Point Clamped (NPC) and Flying Capacitor (FC), and Modular Multilevel Converters (MMC). At this time, a two-level VSC, the most common topology in a low voltage system, is applied.

B. Stability issues in power system

In recent years, the industry has shifted its effort and attention from transient to small-signal stability issue which has emerged as much more critical, primarily to address the modern trend of high levels of Inverter-Based Resources (IBRs) in a power grid [5],[6]

In detail, the instability caused by controller is classified into, depending on the frequency domain, sub-synchronous resonance, near-synchronous resonance, and super-synchronous resonance.

III. DESIGN OF THE NON-LINEAR VSC MODEL

The modeling of VSC is performed with MATLAB/ Simulink. For the simplification of the design, the following assumptions are made in the model design process:

- Three-phase AC voltages of the grid and the PWM-modulated VSC are perfectly balanced, and identical to sinusoidal form through proper filtering.
- The power exchanged with the AC side of VSC is equal to the power exchanged with the DC side of VSC, by ignoring any power loss in VSC.

- A closed-loop dynamic function aims to obtain as close to the first-order response as possible. If the dynamic function is closer to second-order response, an overdamped response is prioritized, or at least, an underdamped response with $\xi > 1/\sqrt{2}$ is considered to limit the over peak.
- VSC follows a cascade control design so that the inner loop operates in at least ten times faster frequency than the outer loop.

The grid is represented by the Thevenin equivalent model, comprised of the voltage source and the impedance shown as
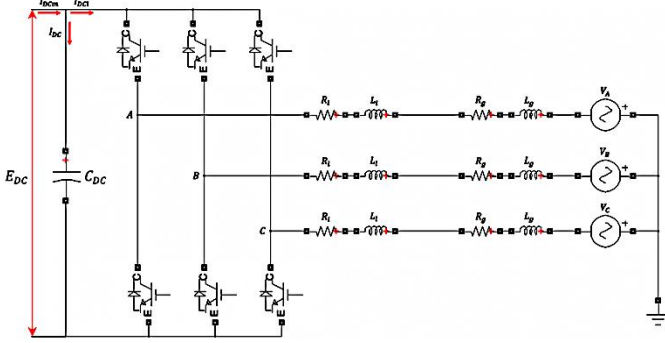

Fig. 1. VSC model to be designed

A. Grid modeling

The short circuit current I_{SC} at the rated voltage V_{Rated}^{P-P} of the system is calculated so that the short circuit power S_{SC}, typically in MVA or KVA, is to be calculated as

$$S_{SC} = E_{gRMS}^{P-N} \cdot I_{SC} = \sqrt{3} \cdot V_{Rated}^{P-P} \cdot I_{SC} = \sqrt{3} \cdot \frac{(V_{Rated}^{P-P})^2}{Z_{SC}} \tag{1}$$

The grid impedance angle ratio seen at the POC is

$$X_L/R \ ratio = \frac{X_L}{R_{POC}} = \frac{1}{10} \tag{2}$$

The Thevenin equivalent of the reactance and the resistance at POC are

$$L_g = \frac{X_{L_g}}{2\pi f} = \frac{E_{gRMS}^{P-N\,2}}{2\pi f \cdot S_{SC}} \tag{3}$$

$$R_g = \frac{1}{X_L/R \ ratio} \cdot X_{L_g} = \frac{1}{10} \cdot \frac{E_{gRMS}^{P-N\,2}}{S_{SC}} \tag{4}$$

B. Equivalent circuit

For the convenience of the design, the simplified equivalent model of the VSC can be implemented with the assumption that PWM create the perfect sinusoidal waveform of AC so that it is represented with a three-phase AC source as
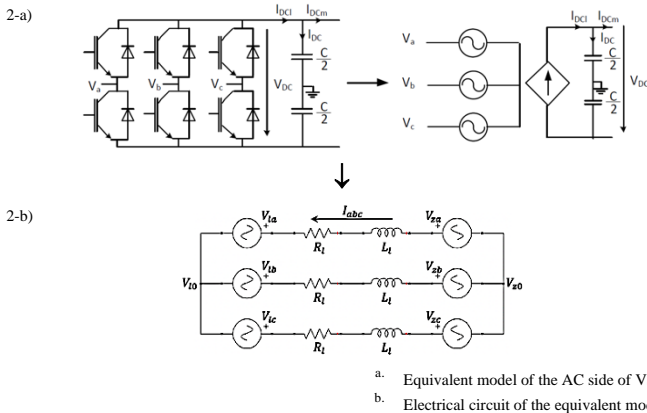
Fig. 2. Grid connected VSC with inductive filtering components; R_l and L_l

$$\begin{bmatrix} v_{zq} \\ v_{zd} \end{bmatrix} - \begin{bmatrix} v_{lq} \\ v_{ld} \end{bmatrix} = \begin{bmatrix} R_l & L_l\omega_e \\ -L_l\omega_e & R_l \end{bmatrix}\begin{bmatrix} i_q \\ i_d \end{bmatrix} + \begin{bmatrix} L_l & 0 \\ 0 & L_l \end{bmatrix}\frac{d}{dt}\begin{bmatrix} i_q \\ i_d \end{bmatrix} \tag{5}$$

v_{zq} and v_{zq} are the grid side $qd0$ voltages, v_{lq} and v_{ld} are the converter side $qd0$ voltages, i_q and i_d are the $qd0$ currents, and ω_e is the electrical angular velocity.

C. Phase Locked Loop (PLL)

Phase Locked Loop (PLL) enables tracking the angle and the angular velocity of the grid for grid synchronization. With the input of the grid voltage in the $qd0$-frame, then the grid angle θ ° is obtained as the output.
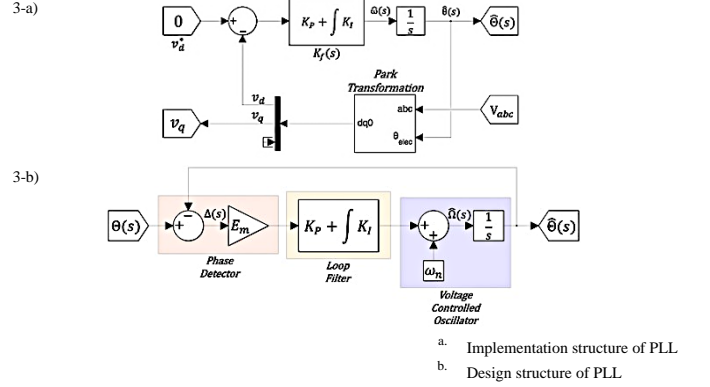
Fig. 3. Phase Locked Loop (PLL) [7]

The design parameters of the PI controller $K_f(s)$ are

$$K_p^{PLL} = \frac{2\zeta_{PLL}\omega_n}{E_m}, \quad K_i^{PLL} = \frac{K_P^{PLL}}{\tau_{PLL}} = \frac{\omega_n^2}{E_m} \tag{6}$$

D. Inner Current Control Loop

The inner loop of the VSC controller controls the currents flowing through the AC side of the convert as well as synchronize them with the grid angle, hence called a current controller. It also allows to track the current reference as the control target which is derived from the outer loop which determines the operation mode.

Recalling that $v_{zd} = 0$ is guaranteed by the PLL, (5) can be rearranged as

$$\begin{bmatrix} v_{zq} \\ 0 \end{bmatrix} - \begin{bmatrix} v_{lq} \\ v_{ld} \end{bmatrix} = \begin{bmatrix} R_l & L_l\omega_e \\ -L_l\omega_e & R_l \end{bmatrix}\begin{bmatrix} i_q \\ i_d \end{bmatrix} + \begin{bmatrix} L_l & 0 \\ 0 & L_l \end{bmatrix}\frac{d}{dt}\begin{bmatrix} i_q \\ i_d \end{bmatrix} \tag{7}$$

For the independent control of the q and the d components, which corresponds to active and reactive power, respectively, the cross coupling terms between q and d components need to be decoupled for their independent control. When outputs of the current controller $\hat{v}_{lq}$ and $\hat{v}_{ld}$ are defined as

$$\begin{bmatrix} \hat{v}_{lq} \\ \hat{v}_{ld} \end{bmatrix} = \begin{bmatrix} R_l & 0 \\ 0 & R_l \end{bmatrix}\begin{bmatrix} i_q \\ i_d \end{bmatrix} + \begin{bmatrix} L_l & 0 \\ 0 & L_l \end{bmatrix}\frac{d}{dt}\begin{bmatrix} i_q \\ i_d \end{bmatrix} \tag{8}$$

The voltages to be applied by converters, v_{lq} and v_{ld}, are arranged in completely decoupled expression by

$$\begin{bmatrix} v_{lq} \\ v_{ld} \end{bmatrix} = \begin{bmatrix} -\hat{v}_{lq} + v_{zq} - L_l\omega_e i_q \\ -\hat{v}_{ld} + L_l\omega_e i_d \end{bmatrix} \tag{9}$$

Then, the transfer functions are derived by applying the Laplace transformation as

$$\frac{\hat{v}_{lq}(s)}{i_q(s)} = \frac{\hat{v}_{ld}(s)}{i_d(s)} = \frac{1}{l_l s + r_l} \tag{10}$$

From the transfer functions, the structures of the inner current control loop is represented in **Fig. 4**.

4-a)

4-b)

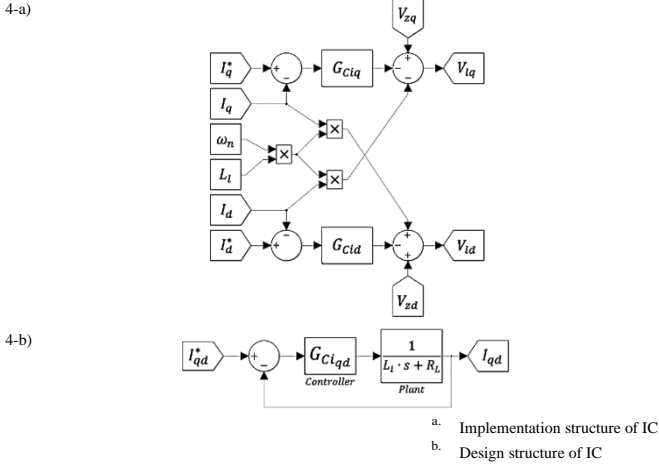a. Implementation structure of IC
b. Design structure of IC

Fig. 4. Inner Current Controller (IC)

Thus, the Laplace expression of the PI controller $G_{C_{iqd}}(s)$ is

$$G_{ciq}(s) = G_{cid}(s) = \frac{K_p^{ic} s + K_i}{s} \qquad (11)$$

and each PI control parameter is written as

$$K_p^{ic} = \frac{L_l}{\tau_{ic}}, \quad K_i^{ic} = \frac{R_l}{\tau_{ic}} \qquad (12)$$
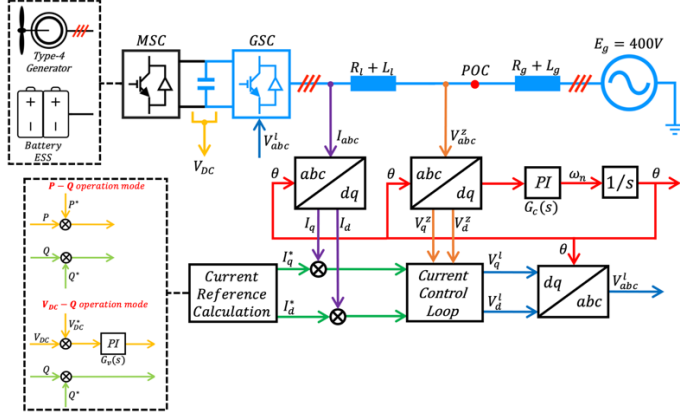
E. Operation mode

Fig. 5. VSC control scheme

1) P-Q operation mode

Depending on which operation mode is to be applied, the DC side of the VSC is modeled differently. Firstly, in the P-Q operation mode, the DC side is considered as an AC voltage source and the reference currents i_{qd}^* are controlled by the straightforward implementation of reference active and reactive power of which the controller is an open loop with the first-order response.

Refer to the instantaneous power theory and the design concept of the PLL which always guarantees $v_{zd} = 0$, each reference current in the P-Q operation mode is simply obtained as:

$$P^* = \frac{3}{2}\left(v_{zq} i_q^* + v_{zd} i_d^*\right) \rightarrow i_q^* = \frac{2P^*}{3v_{zq}} \qquad (13)$$

$$Q^* = \frac{3}{2}\left(v_{zq} i_d^* - v_{zd} i_q^*\right) \rightarrow i_d^* = \frac{2Q^*}{3v_{zq}} \qquad (14)$$

2) V_{DC}-Q operation mode

Secondly, in the Vdc-Q mode, the DC side is considered as a current source and the design of the controller to obtain the reference current i_q^* from the reference DC voltage V_{DC}^* is added. By regulating the DC

voltage of the DC-link capacitor with the external disturbance current I_{DC_m}, active power transmitted between the grid can be controlled.

Refer to **Fig. 1**, when assuming the power exchanged between the AC and the DC side is equal, it can be written as

$$I_{DC_l} = \frac{P_{AC}}{V_{DC}} \qquad (15)$$

$$I_{DC} = I_{DC_l} - I_{DC_m} = C_{dc}\frac{dV_{DC}}{dt} \qquad (16)$$

$$V_{DC} = V_{DC_0} + \frac{1}{C}\int_0^t (I_{DC_l} - I_{DC_m})\, dt \qquad (17)$$

The reference calculation of the DC link voltage adopts the feedback, or a closed-loop, control which is shown in **Fig. 6**.

6-a)

6-b)

a. Implementation structure of DC voltage controller
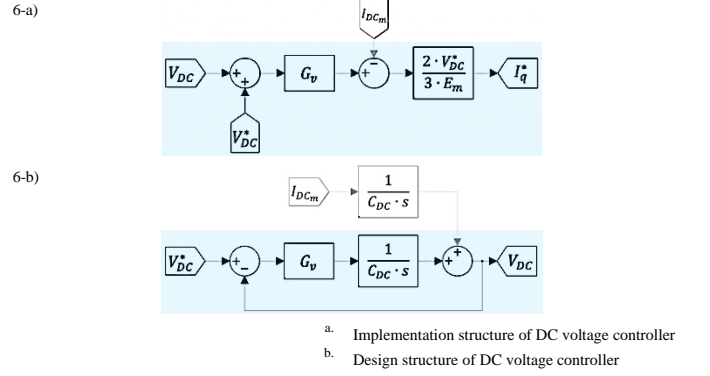b. Design structure of DC voltage controller

Fig. 6. VSC in the P-Q operation mode (IC)

This closed-loop system can be written in the second-order transfer function as

$$V_{dc} = \frac{G_V(s)}{C_{DC}s + G_V(s)}V_{dc}^* + \frac{1}{C_{DC}s + G_V(s)}I_{DC_m} \qquad (18)$$

$$\frac{I_{DC_m}}{V_{dc}^*} = \frac{1}{C_{DC}s + G_V(s)} \quad \leftrightarrow \quad \frac{I_{DC_m}}{V_{dc}^*} = \frac{s}{s^2 + 2\xi_V \omega_V s + \omega_V^2} \qquad (19)$$

When reorganizing (17) to express it based on the term of the PI controller $G_V(s)$, it can be written as (20) whose PI factors are expressed as (21).

$$G_V(s) = \frac{K_p^V s + K_i^V}{s} \quad \leftrightarrow \quad \frac{I_{DC_m}}{V_{dc}^*} = \frac{s}{C_{DC}s^2 + K_p^V s + K_i^V} \qquad (20)$$

$$K_p^V = 2\xi_V \omega_v C_{DC}, \quad K_i^V = \omega_v^2 C_{DC} \qquad (21)$$

In the model, the design parameters of are as follows.

$$\xi_V = \frac{1}{\sqrt{2}} \approx 0.7071 \qquad (22)$$

$$\omega_V = 2\pi \cdot \frac{1}{\tau_{ic}} \cdot \alpha_V = 2\pi \cdot \frac{1}{\tau_{ic}} \cdot 0.05 \qquad (23)$$

α_v is introduced as the proportional factor determining the desired angular velocity of the DC voltage controller ω_v.

F. The non-linear model in MATLAB/Simulink

The grid, AC side of the converter, PLL, and IC are in common regardless of the operation mode.

In the P-Q operation mode, the qd-reference currents are from active and reactive power which are directly fed into the system.

In the V_{DC}-Q operation mode, however, the q-reference current is controller with the added PI-controller, $G_V(s)$. Also, the DC side equivalent circuit is added including the capacitor, C_{DC}. Therefore, the bus where the AC power and DC power are equal is included with the assumption that any losses are to be neglected.
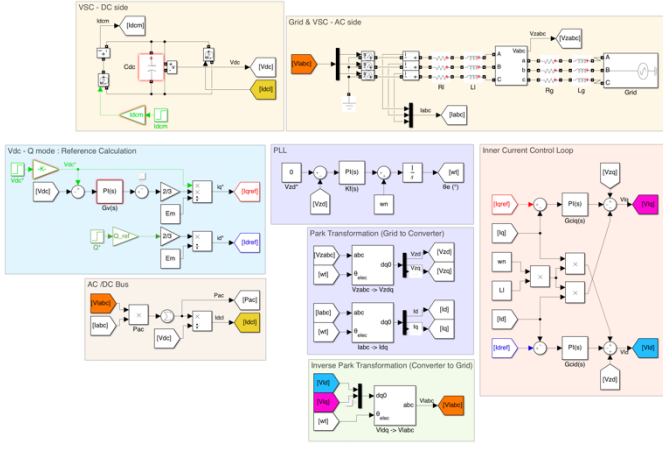
3

Fig. 7. The non-linear model of VSC with the V_{DC}-Q operation mode

IV. LINEAR MODEL

For clarity of a control without confusion, a linear system is preferred to a nonlinear system. Thus, the non-linear model is to be linearized for the linear model design.

A. Phase Locked Loop (PLL)

The state-space of the PLL is separated into two sub-blocks. The first block corresponds to the loop filter to make the error between the reference and the measured value zero.

$$\frac{d}{dt}\begin{bmatrix}\int \Delta v_{zd}^* \\ \int \Delta v_{zd}\end{bmatrix} = \begin{bmatrix}0 & 0 \\ 0 & 0\end{bmatrix}\begin{bmatrix}\int \Delta v_{zd}^* \\ \int \Delta v_{zd}\end{bmatrix} + \begin{bmatrix}1 & 0 \\ 0 & 1\end{bmatrix}\begin{bmatrix}\Delta v_{zd}^* \\ \Delta v_{zd}\end{bmatrix}[\Delta\theta]$$

$$[\Delta\omega] = [K_i^{PLL} \quad -K_i^{PLL}]\begin{bmatrix}\int \Delta v_{zd}^* \\ \int \Delta v_{zd}\end{bmatrix} + [K_p^{PLL} \quad -K_p^{PLL}]\begin{bmatrix}\Delta v_{zd}^* \\ \Delta v_{zd}\end{bmatrix}$$

(24)

The second block represents the voltage-controlled oscillator whose input is $\Delta\omega$ and the output is $\Delta\theta$.

$$\frac{d}{dt}[\Delta\theta] = [0]\cdot[\Delta\theta] + [1]\cdot[\Delta\omega]\begin{bmatrix}\Delta v_{lq} \\ \Delta v_{ld}\end{bmatrix}$$

$$[\Delta\theta] = [1]\cdot[\Delta\theta] + [0]\cdot[\Delta\omega]$$

(25)

B. Inner Current Control Loop

The state-space of IC is presented as

$$\frac{d}{dt}\begin{bmatrix}\int \Delta i_q^{c*} \\ \int \Delta i_d^{c*} \\ \int \Delta i_q^c \\ \int \Delta i_d^c\end{bmatrix} = \begin{bmatrix}0 & 0 & 0 & 0 \\ 0 & 0 & 0 & 0 \\ 0 & 0 & 0 & 0 \\ 0 & 0 & 0 & 0\end{bmatrix}\begin{bmatrix}\int \Delta i_q^{c*} \\ \int \Delta i_d^{c*} \\ \int \Delta i_q^c \\ \int \Delta i_d^c\end{bmatrix} + \begin{bmatrix}1 & 0 & 0 & 0 & 0 & 0 \\ 0 & 1 & 0 & 0 & 0 & 0 \\ 0 & 0 & 1 & 0 & 0 & 0 \\ 0 & 0 & 0 & 1 & 0 & 0\end{bmatrix}\begin{bmatrix}\Delta i_q^{c*} \\ \Delta i_d^{c*} \\ \Delta i_q^c \\ \Delta i_d^c \\ \Delta v_q^z \\ \Delta v_d^z\end{bmatrix}$$

(26)

$$\begin{bmatrix}\Delta v_{lq} \\ \Delta v_{ld}\end{bmatrix} = \begin{bmatrix}-K_i^{ic} & 0 & K_i^{ic} & 0 \\ 0 & K_i^{ic} & 0 & K_i^{ic}\end{bmatrix}\begin{bmatrix}\int \Delta i_q^{c*} \\ \int \Delta i_d^{c*} \\ \int \Delta i_q^c \\ \int \Delta i_d^c\end{bmatrix} + \begin{bmatrix}-K_p^{ic} & 0 & K_p^{ic} & -\omega_n L & 1 & 0 \\ 0 & -K_p^{ic} & \omega_n L & K_p^{ic} & 0 & 1\end{bmatrix}\begin{bmatrix}\Delta i_q^{c*} \\ \Delta i_d^{c*} \\ \Delta i_q^c \\ \Delta i_d^c \\ \Delta v_q^z \\ \Delta v_d^z\end{bmatrix}$$

C. Grid-connected VSC with L −filter

One difference from the state-space model is that V_{z0} of the non-linear model is measured at POC, at which the point is after R_g and L_g. However, v_{qd}^z is the grid level voltages measured before R_g and L_g. Therefore, the matrixes of A, B, C, and D for the state-space $'filterL'$ differ from those of the non-linear model

$$\frac{d}{dt}\begin{bmatrix}\Delta i_q^c \\ \Delta i_d^c\end{bmatrix} = \begin{bmatrix}-\frac{r_{gl}}{L_{gl}} & -\omega_n \\ \omega_n & -\frac{r_{gl}}{L_{gl}}\end{bmatrix}\begin{bmatrix}\Delta i_q^c \\ \Delta i_d^c\end{bmatrix} + \begin{bmatrix}-\frac{1}{L_{gl}} & 0 & \frac{1}{L_{gl}} & 0 \\ 0 & -\frac{1}{L_{gl}} & 0 & \frac{1}{L_{gl}}\end{bmatrix}\begin{bmatrix}\Delta v_q^c \\ \Delta v_d^c \\ \Delta v_q^z \\ \Delta v_d^z\end{bmatrix}$$

(27)

$$\begin{bmatrix}\Delta i_q^c \\ \Delta i_d^c \\ \Delta v_q^z \\ \Delta v_d^z\end{bmatrix} = -\begin{bmatrix}1 & 0 \\ 0 & 1 \\ \frac{r_g L_l - r_l L_g}{L_{gl}} & 0 \\ 0 & \frac{r_g L_l - r_l L_g}{L_{gl}}\end{bmatrix}\begin{bmatrix}\Delta i_q^c \\ \Delta i_d^c\end{bmatrix} + \begin{bmatrix}0 & 0 & 0 & 0 \\ 0 & 0 & 0 & 0 \\ \frac{L_g}{L_{gl}} & 0 & \frac{L_l}{L_{gl}} & 0 \\ 0 & \frac{L_g}{L_{gl}} & 0 & \frac{L_l}{L_{gl}}\end{bmatrix}\begin{bmatrix}\Delta v_q^c \\ \Delta v_d^c \\ \Delta v_q^z \\ \Delta v_d^z\end{bmatrix}$$

D. Conversion for angle rotation

1) Converter voltages conversion by $T^{-1}(\theta)$

Since the current controller outputs follow the converter reference, the inverse Park transformation rotates by $\Delta\theta$ is applied to transform the output of the state-space $'ic'$, from the converter reference to the grid references. Applying the linearization process, the expression of the transformation is

$$\begin{bmatrix}\Delta v_q^c \\ \Delta v_d^c\end{bmatrix} = \begin{bmatrix}0 \\ 0\end{bmatrix}[\quad] + \begin{bmatrix}\cos\theta_e & \sin\theta_e & -\sin\theta_e\cdot v_{q0}^{cc} + \cos\theta_e\cdot v_{d0}^{cc} \\ -\sin\theta_e & \cos\theta_e & -\cos\theta_e\cdot v_{q0}^{cc} - \sin\theta_e\cdot v_{d0}^{cc}\end{bmatrix}\begin{bmatrix}\Delta v_q^{cc} \\ \Delta v_d^{cc} \\ \Delta\theta\end{bmatrix}$$

(28)

$\Delta\theta = \theta_{cc} - \theta_c = \theta_{cc}$, as the grid reference angle $\theta_c = 0\,°$ by the PLL, and θ_e is the error of the angle, which is very close to 0, between the desired and the actual angle which is set to $\theta_e = 10^{-36}\,°$.

2) Grid voltages conversion by $T(\theta)$

The outputs of the state-space $'filterL'$ follows the grid reference. Therefore, they need to be converted from the grid to the converter reference to be input to the state-space $'ic'$. by the Park transformation rotates by $\Delta\theta$.

$$\begin{bmatrix}\Delta i_q^{cc} \\ \Delta i_d^{cc}\end{bmatrix} = \begin{bmatrix}0 \\ 0\end{bmatrix}[\quad] + \begin{bmatrix}\cos\theta_e & -\sin\theta_e & -\sin\theta_e\cdot i_{q0}^c - \cos\theta_e\cdot i_{d0}^c \\ \sin\theta_e & \cos\theta_e & \cos\theta_e\cdot i_{q0}^c - \sin\theta_e\cdot i_{d0}^c\end{bmatrix}\begin{bmatrix}\Delta i_q^c \\ \Delta i_d^c \\ \Delta\theta\end{bmatrix}$$

(29)

3) Grid currents conversion by $T(\theta)$

The same method is applied to the transformation of i_{qd}^{cc} to i_{qd}^c as

$$\begin{bmatrix}\Delta i_q^c \\ \Delta i_d^{cc}\end{bmatrix} = \begin{bmatrix}0 \\ 0\end{bmatrix}[\quad] + \begin{bmatrix}\cos\theta_e & -\sin\theta_e & -\sin\theta_e\cdot i_{q0}^c - \cos\theta_e\cdot i_{d0}^c \\ \sin\theta_e & \cos\theta_e & \cos\theta_e\cdot i_{q0}^c - \sin\theta_e\cdot i_{d0}^c\end{bmatrix}\begin{bmatrix}\Delta i_q^c \\ \Delta i_d^c \\ \Delta\theta\end{bmatrix}$$

(30)

E. AC/DC Bus

The linearization of active and reactive power equations can be derived as

$$P = \frac{3}{2}\left(v_q i_{q0} + v_{q0} i_q + v_d i_{d0} + v_{d0} i_d\right)$$

(31)

$$Q = \frac{3}{2}\left(v_q i_{q0} + v_{q0} i_q - v_d i_{d0} - v_{d0} i_d\right)$$

(32)

Then, the state-space of the power exchanged between the AC and the DC side can be expressed as

$$\frac{d}{dt}[\Delta v_{dc}] = \left[-\frac{P_{c0}}{C_{dc}\cdot v_{dc0}^2}\right][\Delta v_{dc}] + \left[\frac{1}{C_{dc}} \quad \frac{3v_{q0}^{cc}}{2C_{dc}v_{dc0}} \quad \frac{3v_{d0}^{cc}}{2C_{dc}v_{dc0}} \quad \frac{3i_{q0}^c}{2C_{dc}v_{dc0}} \quad \frac{3i_{d0}^c}{2C_{dc}v_{dc0}}\right]\begin{bmatrix}\Delta i_{dcm} \\ \Delta i_q^{cc} \\ \Delta i_d^c \\ \Delta v_q^c \\ \Delta v_d^c\end{bmatrix}$$

(33)

$$\begin{bmatrix}\Delta v_{dc} \\ \Delta i_{dcl}\end{bmatrix} = \begin{bmatrix}1 \\ -\frac{P_{c0}}{v_{dc0}^2}\end{bmatrix}[\Delta v_{dc}] + \begin{bmatrix}0 & 0 & 0 & 0 & 0 \\ 0 & \frac{3v_{q0}^{cc}}{2v_{dc0}} & \frac{3v_{d0}^{cc}}{2v_{dc0}} & \frac{3i_{q0}^c}{2v_{dc0}} & \frac{3i_{d0}^c}{2v_{dc0}}\end{bmatrix}\begin{bmatrix}\Delta i_{dcm} \\ \Delta i_q^{cc} \\ \Delta i_d^{cc} \\ \Delta v_q^c \\ \Delta v_d^c\end{bmatrix}$$

(34)

F. Operation mode

1) P-Q operation mode

The SSM applied in the P-Q mode is same as that of which A, B, and C matrix are all zero matrices, and D matrix is the gain whose value is $\frac{2}{3E_m}$.

2) V_{DC}-Q operation mode

The expression of VDC-Q mode in state-space form is

$$\frac{d}{dt}\begin{bmatrix} \int v_{dc}^* \\ \int v_{dc} \end{bmatrix} = \begin{bmatrix} 0 & 0 \\ 0 & 0 \end{bmatrix}\begin{bmatrix} \int v_{dc}^* \\ \int v_{dc} \end{bmatrix} + \begin{bmatrix} 1 & 0 \\ 0 & 1 \end{bmatrix}\begin{bmatrix} v_{dc}^* \\ v_{dc} \end{bmatrix}$$

$$[i_q^*] = \begin{bmatrix} \frac{2v_{dc}^*}{3E_m}K_i^v & -\frac{2v_{dc}^*}{3E_m}K_i^v \end{bmatrix}\begin{bmatrix} \int v_{dc}^* \\ \int v_{dc} \end{bmatrix} + \begin{bmatrix} \frac{2v_{dc}^*}{3E_m}K_p^v & -\frac{2v_{dc}^*}{3E_m}K_p^v \end{bmatrix}\begin{bmatrix} v_{dc}^* \\ v_{dc} \end{bmatrix} \quad (35)$$

G. The linear model in MATLAB/Simulink

In the P-Q mode, each variation in active and reactive power is feed-forwarded to the current controller in the form of a current calculated by dividing each power by $3/2 \cdot E_m$. The number of the state-spaces and eigenvalues of the P-Q operation mode is 8.

In the V$_{DC}$-Q mode, depending on the variation of I_{DC_m}, the value of V_{DC} changes which results in the change of the reference current $i_q^{c\,*}$. The procedure to calculate $i_q^{c\,*}$ is exactly same to that of the P-Q operation mode, the feedforward implementation. As a result, due to the addition of the state-space block v_{DC}, the number of state-spaces and eigenvalues in the V$_{DC}$-Q operation mode is 9.
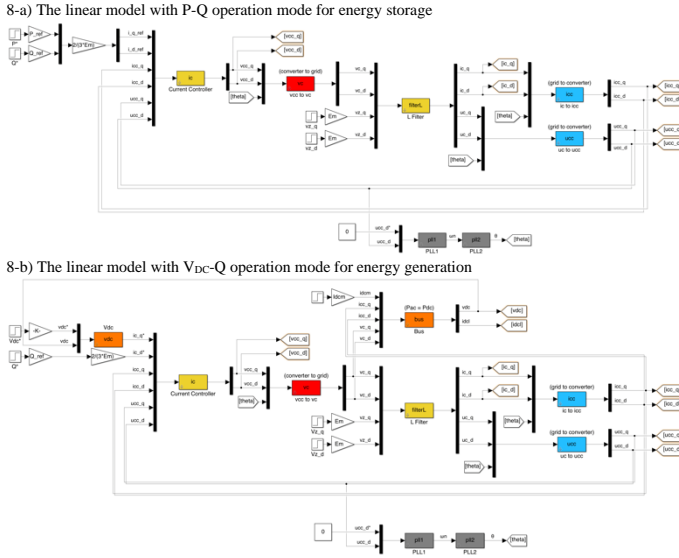
8-a) The linear model with P-Q operation mode for energy storage

8-b) The linear model with V$_{DC}$-Q operation mode for energy generation

Fig. 8. The linear VSC model with two different operation modes

V. VALIDATION OF THE LINEAR MODEL

The results from two simulations of the linear and the nonlinear model with two operation mode, of which the section is from $1.995\ sec$ to $2.05\ sec$. The first case is that I_{DCm} has the step variable of 1 % for the active power variation, and the second case is 1 % step-up of Q is applied for the reactive power variation. In **Fig. 9**, it is observed that the currents and voltages in qd-frame from two models are exactly matched which validates the linearization of the non-linear VSC model within the simulation time is successful.
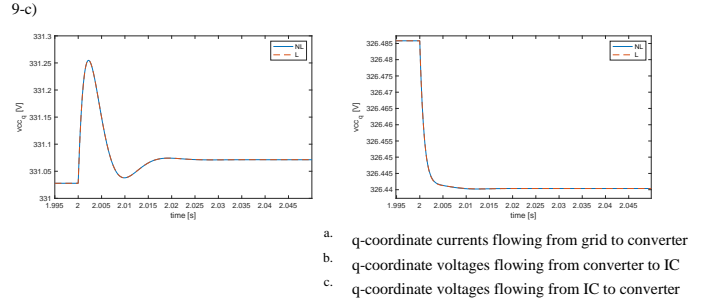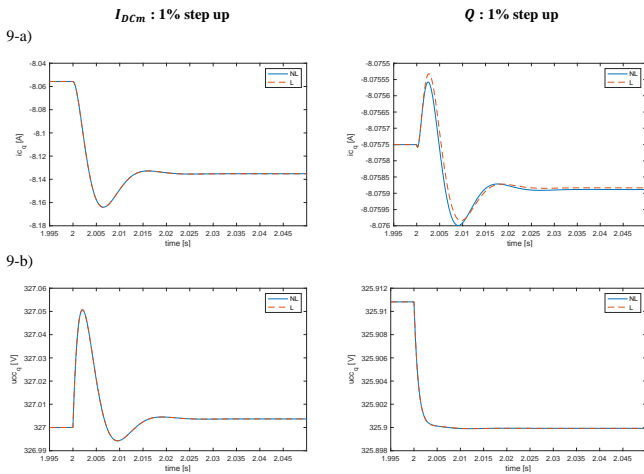
9-a)

9-b)

9-c)

a. q-coordinate currents flowing from grid to converter
b. q-coordinate voltages flowing from converter to IC
c. q-coordinate voltages flowing from IC to converter

Fig. 9. Comparision of two simulation results for the linearization validation

VI. CASE STUDIES AND COMPARISON

A. Changes in Control Parameters

1) Short Circuit Power, S_{SC}

The decrease in S_{sc} results in the increase in L_g and R_g, which is defined as a weak grid. As the grid impedances increase, the oscillation amplitudes of voltages and currents increase.
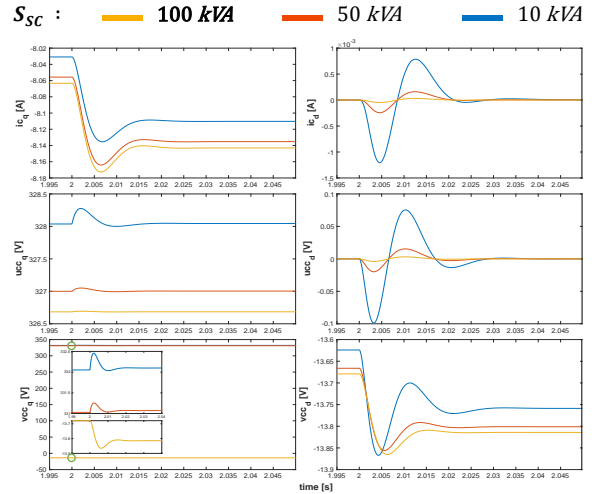

Fig. 10. Simulation results when S$_{SC}$ changes

2) Time constant of IC, τ_{ic}

As τ_{ic} increases, the settling time t_{SS} for current i_{qd}^c and voltages v_{qd}^{cc} and u_{qd}^{cc}, to reach the steady-state becomes larger. However, the larger the value of τ_{ic}, the smaller the peak value of current i_{qd}^c while the larger the peak value of voltages v_{qd}^{cc} and u_{qd}^{cc}.
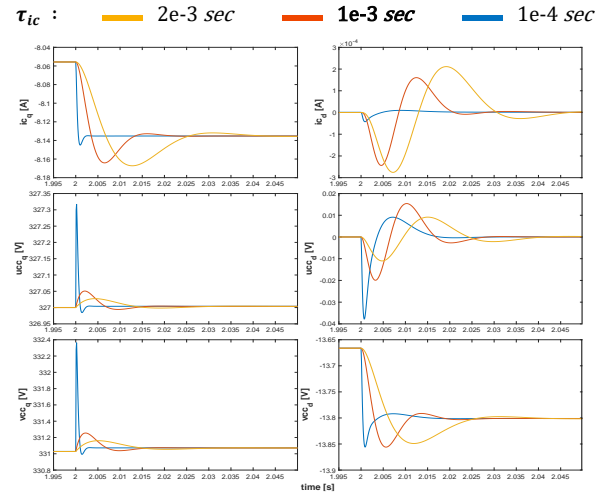

Fig. 11. Simulation results when τ_{ic} changes

3) Grid nominal frequency, ω_n

As ω_n increases, the overshoot is expected to increase. In the case of i_{qd}^c and v_{qd}^{cc}, the prediction is true, but u_{qd}^{cc} exceptionally decreases the overshoot.
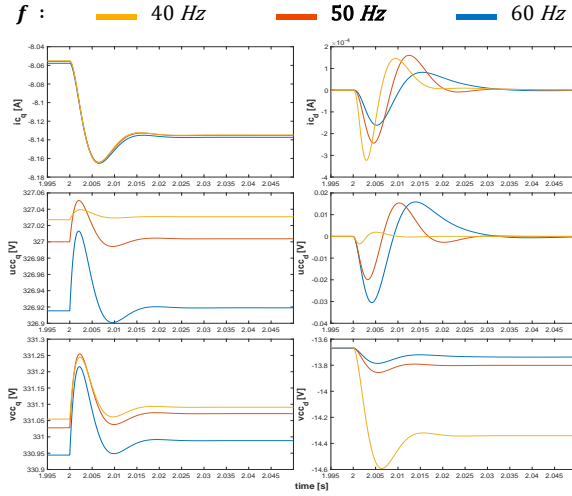

Fig. 12. Simulation results when ω_n changes

4) DC voltage control frequency, ω_V

As ω_V increases, so do the gain parameters K_p^V and K_i^V which cause the maximum oscillation larger and settles faster as α_V increases.

5) Damping ratio of PLL, ξ_{PLL}

The significant effects of increasing ξ_{PLL} are the increases in τ_{PLL}, and K_p^{PLL}. This results in a larger overshoot and the increase of the settling time in the d-coordinate i_d^c, v_d^{cc}, and u_d^{cc} as ξ_{PLL} decreases.
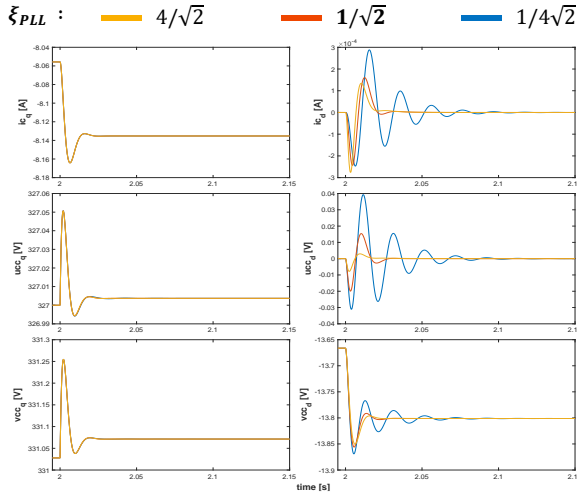

Fig. 13. Simulation results when ξ_{PLL} changes

6) Damping ratio of DC voltage controller, ξ_V

The damping ratio of the DC voltage controller ξ_V is proportional to K_p^V and affects current i_{qd}^c, voltages v_{qd}^{cc} and u_{qd}^{cc} in the $dq-$coordinate. The currents and the voltages tend to oscillate faster as ξ_V increases. However, regarding overshoots, the $d-$coordinate current i_d^c and the $q-$coordinate voltages v_q^{cc} and u_q^{cc} have larger overshoots whereas the others have smaller overshoots in the same condition at which ξ_V increases.

B. Eigenvalue Analysis

1) Short Circuit Power, S_{SC}

The change of eigenvalues when S_{sc} varies from 10 times to 0.12 times the initial value of $100\ kVA$. Eigenvalues move toward left as S_{sc} decreases, which causes larger overshoot with slower response of oscillation. The most important result is that λ_1 and λ_2 come to have the real positive parts, implying the grid system become unstable as grid impedance increases.
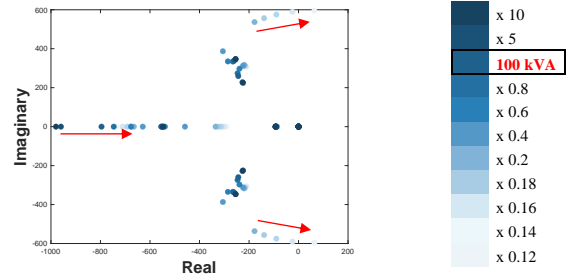

Fig. 14. Eigenvalues when S_{SC} changes

2) Time constant of IC, τ_{ic}

It is seen that the change of τ_{ic}, from 5 times to 0.05 times the initial value of $0.001\ sec$, does not affect the stability.

However, the significance of the figure is the radical movement of the pair of the poles. A vertical direction that the absolute value of the imaginary part increases means the overshoot is increasing but the envelop is the same. Moreover, it also moves a bit to the left so the envelop of the oscillation is affected by the change in τ_{ic}.

In addition, the rapid movement in a horizontal direction to the left which the real part decreases, yields the response damps out faster as τ_{ic} decreases when the frequency is constant.
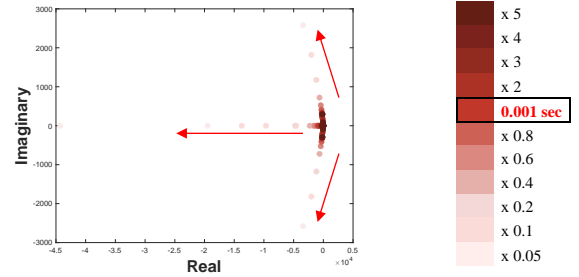

Fig. 15. Eigenvalues when τ_{ic} changes

3) Grid nominal frequency, ω_n

The observation when ω_n changes from 7.25 times to 0.5 times the initial value, of which is $2 \cdot \pi \cdot 50 \approx 314.1592\ rad/s$ is presented.

There are two of remarkable pairs moving toward 0 with decrease in real and imaginary parts. The radial movements of these two sets of poles verifies the trend, which is the variation in overshoots and the faster oscillation response as ω_n decreases.
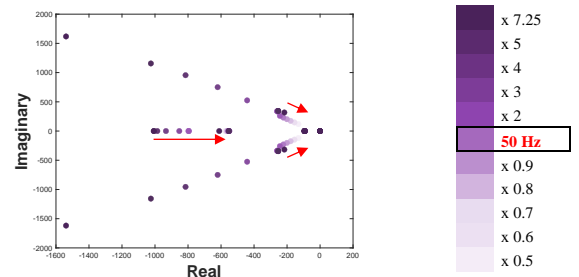

Fig. 16. Eigenvalues when ω_n changes

6

4) DC voltage control frequency, ω_V

The change of α_V which is ω_V is proportional to ω_V gives the transitions of eigenvalues when the frequency of the DC voltage controller changes from 4 times to 0.01 times the initial value of ω_V when $\alpha_V = 0.05$.

Observing the eigenvalues' trend as ω_V decreases, one of pairs of eigenvalues head to the origin and it proves the more rapid system response, and it is induced that the other eigenvalue moving left along the real axis brings out the increase in overshoot.

When ω_V decreases until its value become 0.01 times the initial value, λ_5 and λ_6 come to have positive real parts, so the system is unstable.
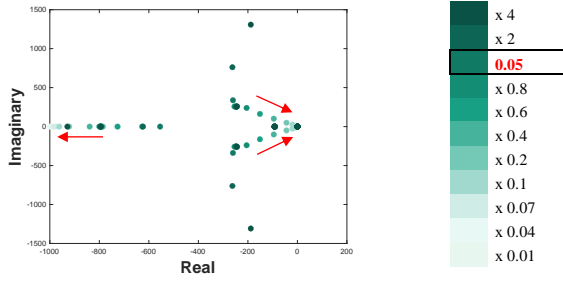
Fig. 17. Eigenvalues when ω_V changes

5) Damping ratio of PLL, ξ_{PLL}

In **Fig. 18**, the movements of eigenvalues when ξ_{PLL} changes from 4 time to 0.03 times the initial value of $1/\sqrt{2}$ are plotted.

The instability of the system is found from the positive real values of λ_3 and λ_4 when ξ_{PLL} become less than or equal to 0.04 times its initial value.

Considering the result from **Fig. 13**, another pair of eigenvalues moving toward left along the real part axis would represent the increasing overshoot and slower response of the system as ξ_{PLL} decreases.
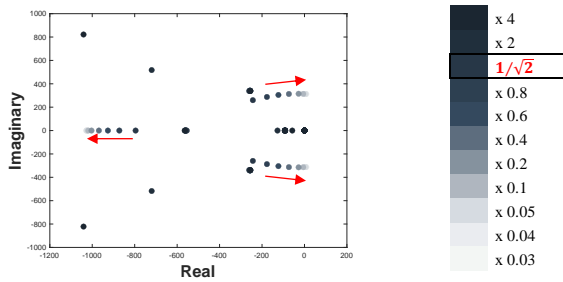
Fig. 18. Eigenvalues when ξ_{PLL} changes

6) Damping ratio of DC voltage controller, ξ_V

First, it is obvious that the system becomes unstable when ξ_V less than or equal to 0.2 times the initial value of $1/\sqrt{2}$ by the pair of eigenvalues, λ_5 and λ_6.

Second, the movement of a pair of eigenvalues along the radial line to the direction which both the absolute values of the real and the imaginary parts decrease brings out slower response and oscillation for longer times.

Lastly, the movement of the poles to the left along the real part axis as means the decrease in overshoot, nevertheless the dynamic behavior when the damping ratio decreases brings out the increase of overshoot, which cannot be determined only by the results from **Fig. 19**.
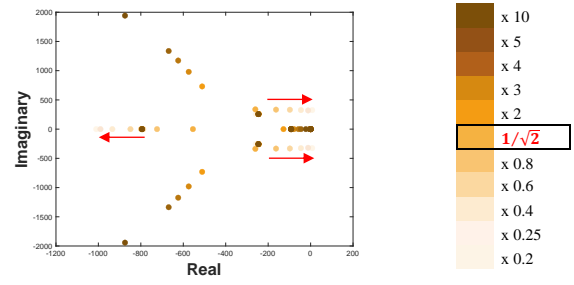
Fig. 19. Eigenvalues when ξ_V changes

C. Bode Plot Analysis

1) Short Circuit Power, S_{SC}

In Y_{qq}, the magnitude is constant, but starts to increase from a frequency region of $10\,Hz$ or higher to have a maximum magnitude around $320\,Hz$. As S_{sc} decreases, the value of the frequency reaching the maximum magnitude decreases. Similarly, the phase change in Y_{qq} keeps constant but become negative when frequency becomes larger than $10\,Hz$ implying the output i_q^c is lagging the input v_q^z.

Different from Y_{qq}, in case of Y_{qd}, Y_{dq}, and Y_{dd}, the frequency at which the magnitude has a maximum value increases as S_{sc} decreases from $100\,kVA$ to $50\,kVA$ and $10\,kVA$. Each of significant change of the phase in Y_{qd}, Y_{dq}, and Y_{dd} is at the frequency around $30\,Hz$, of which the phase difference has a maximum value.

As a consequence of **Fig. 20**, Y_{qq} is the least affected while Y_{dq} is the most affected by the change in S_{sc}.
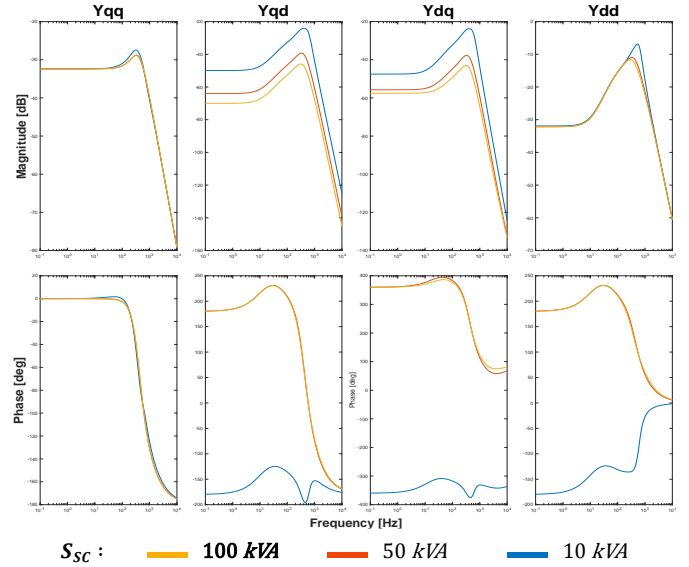
Fig. 20. Bode plot – admittance Y when S_{SC} changes

2) Time constant of IC, τ_{ic}

The greater the value of τ_{ic}, the greater the peak value of both the magnitude and the phase. Also, as τ_{ic} increases, the value of the frequency reaching the maximum magnitude and phase becomes lower.

As τ_{ic} increases, the section of the frequency where the magnitude and the phase change become wider, requiring the consideration of dynamic responses of the system in wider range of frequencies.

The most drastic change in the magnitude and the phase is observed in Y_{dd}, whereas the most moderate change is observed in Y_{qq}.
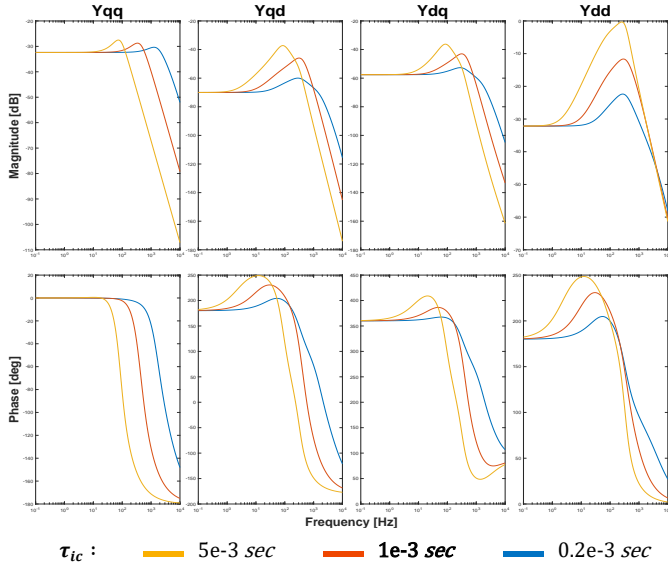
Fig. 21. Bode plot - admittance Y when τ_ic changes

3) Grid nominal frequency, ω_n

In **Fig. 22**, except for Y_{dq}, it is seen that the influence of the change in ω_n on the admittance is less noticeable than other parameters. Still, it is observed that the increase of ω_n brings out the increase of the maximum magnitude and phase as well as the frequency at which is the point.

Y_{dq} is showing quite a different response from other three. In the magnitude, the increase in frequency causes higher constant value at lower frequency range from 10^{-1} Hz to 10 Hz and gentle slope at higher frequency from 300 Hz to 10 kHz. Its phase difference become closer to 0° as ω_n differs.
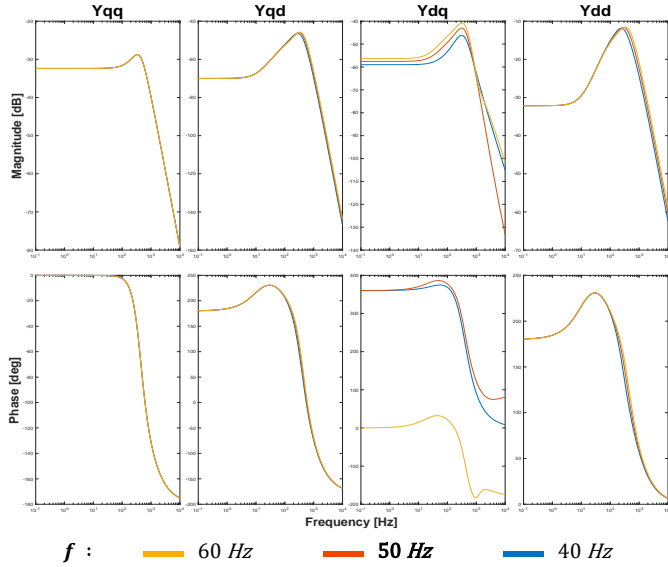

Fig. 22. Bode plot - admittance Y when ω_n changes

4) DC voltage control frequency, ω_V

In **Fig. 23**, it is firstly found that Y_{dd} is nearly affected by ω_V.

Looking into Y_{qq}, its responses of the magnitude and the phase keep in constant at lower frequency from 10^{-1} Hz to 20 Hz. In higher frequency range, the magnitude increases more rapidly until it reaches the peak, at which the frequency is higher as ω_V increases. After taking each vertex, the magnitude of Y_{qq} decreases with almost equal slope, maintaining the difference between cases of different ω_V. When it

comes to the phase change of Y_{qq}, it shows an exponential response when α_V is 0.1 or 0.05. However, in case of $\alpha_V = 0.025$, the phase response shows a product of a linear function and an exponential function, $ax \cdot e^x$.

The trend of magnitudes found in the crossing terms of admittances Y_{qd} and Y_{dq} is that the frequency at which the peak magnitude exists becomes smaller as α_V decreases. The change of phases of Y_{qd} and Y_{dq} take the form of a product of a quadradic function and an exponential function, $ax^2 \cdot e^x$, while the average of the phase difference is larger when the value of α_V is larger.
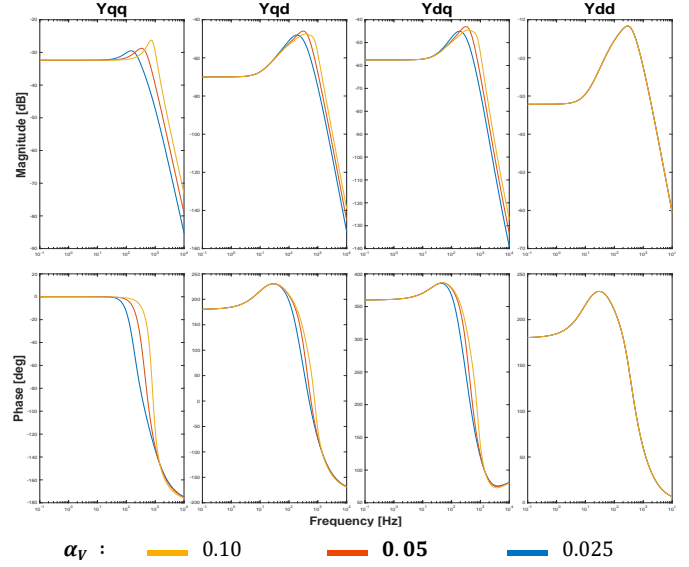

Fig. 23. Bode plot - admittance Y when ω_V changes

5) Damping ratio of PLL, ξ_{PLL}

The change in Y_{qq} depending on the increase or decrease of ξ_{PLL} is the smallest. In the lower frequency from 10^{-1} Hz to 10 Hz, there is no variety of change in magnitudes. Different from Y_{qd}, Y_{dq}, and Y_{dd} which have larger peak values of magnitude when ξ_{PLL} is smaller, the larger the ξ_{PLL}, the larger the resonant peak in Y_{qq}.

In case of Y_{qd}, Y_{dq}, and Y_{dd}, the magnitudes increase until they reach each resonant peak at the frequency between 300 Hz and 400 Hz. After the peak point, the smaller the ξ_{PLL}, the faster the magnitude decreases, and finally, in the higher frequency region of 400 Hz or higher, there is an intersection at frequency between 450 Hz to 470 Hz where the magnitude for the 4 times the initial value of ξ_{PLL} is the largest.

The phase derivation of Y_{qq} is exactly the same regardless of the change in ξ_{PLL}. Also, in Y_{qd} and Y_{dd}, the larger ξ_{PLL} increases the phase, whereas in Y_{dq}, the smaller ξ_{PLL} increases the phase.

6) Damping ratio of DC voltage controller, ξ_V

In **Fig. 24**, different from the case of ξ_{PLL}, Y_{dd} is the least affected by ξ_V showing very small derivative of magnitude and no change in phase derivation. Still, each magnitude keeps constant at lower frequency and starts to increase until it come to the peak point, and then, starts decreasing.

The resonant peaks of magnitude and phase is larger as ξ_V is smaller in all admittances. After the peak point, the smaller the ξ_V, the faster the magnitude decreases, so the order of the magnitude values according to ξ_V is reversed.

A common finding in the phase change of the four admittances is that the smaller ξ_V is, the larger the peak value of the phase is.

8

The phase of Y_{qq} is constant in lower frequency from $10^{-1}\,Hz$ to $30\,Hz$ and then it decreases in exponential form. At the admittances Y_{qd} and Y_{dq}, a phase change is detected over all frequency ranges.
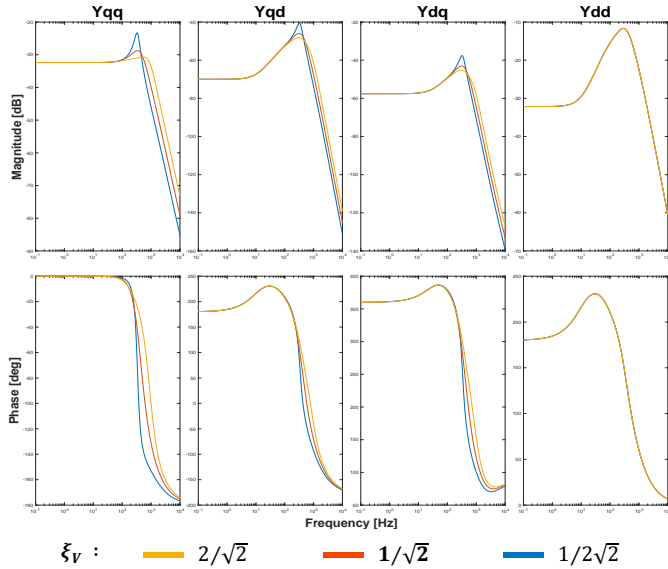

Fig. 24. Bode plot - admittance Y when ξ_V changes

VII. Conclusion

A. Review of the results

The results of **VI.A** show how the control parameters affect the control of currents and voltages of the designed VSC model and represent how the system could be analyzed based on the consideration of the impact of the integral and the proportional factor of a PI controller on the response of oscillations of currents and voltages of the system.

In **VI.B**, the changes of eigenvalues with respect to the change in each parameter are investigated. The transition of eigenvalues manifests the stability of the system, finding the instability cases with the decrease in the value of each parameter, S_{SC}, ω_V, ξ_{PLL}, and ξ_{PLL}. Although no stability issues have been found with the respect to the observed range of ω_n, the movement of the two eigenvalues towards the imaginary axis suggest the possibility of them to have positive real part, which implies the instability of the system. However, τ_{ic} is the only parameter to be concluded that it does not affect the stability when considering the movements of all eigenvalues heading to the left or upward, bringing out more rapid damping with larger overshoot.

In **VI.C**, the impedance-based representation of the system is analyzed through the Bode plot showing the magnitude and the phase change of admittances with frequency. The system response was analyzed by dividing the section into three frequency ranges. The focus was on which frequencies the magnitude and the phase have their maximum values and how the magnitude and the phase are affected when each parameter increases and decreases. Notable changes occurred mainly in the cross terms, Y_{qd} and Y_{qd}, except for τ_{ic} in which all four admittance changes were clearly visible. For example, there were little change in Y_{qq} regardless of the increase or the decrease of ω_n and ξ_{PLL}, while little change in Y_{dd} was found for the variation of ω_V and ξ_V. Another finding from the results is that the magnitude of admittance is greater as S_{SC}, ξ_{PLL}, and ξ_V are small, and τ_{ic}, ω_n, and ω_V are large.

B. Completion and Discussion

The eigenvalue analysis, or the root locus analysis tracking the movement of eigenvalues for the stability analysis, has proved its simplicity and feasibility as a tool to analyze the impact of the designed VSC model on the grid. Nevertheless, the need for detailed design specifications of the controller is still a big disadvantage considering the current industry situation presented in **I**.

In this Master thesis, the designs of the VSC models are based on the d-q domain and so does the impedance-based analysis. It has often been thought that d-q Impedance method has the disadvantage that Nyquist criterion for a Single-Input Single-Output (SISO) system and bode plots cannot be used for the stability analysis of three-phase AC systems [8], which can be overcome with symmetric systems using a complex representation.

Therefore, by modeling the linear model with the state-space method, stated in **IV**, the disadvantage of d-q domain model has been eliminated, while maintaining its advantage of supporting a Multi-Input Multi-Output (MIMO) system. In other words, the applied method meets the purpose of presenting a reliable data-driven stability analysis method in power systems without detailed design specifications of power electronics by regarding subsystems as a black-box which does not require for any knowledge on control parameters.

Also, the results have proved obviously that impedance-based analysis is useful enough to deal with the grid stability problem related to high levels of power electronics, due to its easiness to observe the derivatives of magnitude and phase in relation to voltage and current with respect to a wide range of frequencies just in a single plot as well as the convenience of the measurement of voltages and currents at any point to be inspected by power system operators.

Nevertheless, neither the eigenvalue analysis nor the impedance-based representation in this master thesis do not provide information about which and how much each state variable of the control system affects the system when its step variation is given. The investigation of the participation factors can supplement such a problem. Also, the perfect design should consider the effects of the modulation process to convert DC to AC producing harmonics and imperfect sinusoidal waveshapes which affect the result of the stability analysis. However, the significance of the master thesis lies on proving the validity of the impedance-based stability analysis in the industrial field by presenting the procedure for designing the average VSC model and comparing its results with the impedance-based analysis and the eigenvalue analysis.

VIII. Bibliography

[1] G. Venkataramanan and C. Marnay, "A larger role for microgrids," in IEEE Power and Energy Magazine, vol. 6, no. 3, pp. 78-82, May-June 2008, doi: 10.1109/MPE.2008.918720.

[2] B. Kroposki, R. Lasseter, T. Ise, S. Morozumi, S. Papathanassiou and N. Hatziargyriou, "Making microgrids work," in IEEE Power and Energy Magazine, vol. 6, no. 3, pp. 40-53, May-June 2008, doi: 10.1109/MPE.2008.918718.

[3] S. Shah, P. Koralewicz, V. Gevorgian, H. Liu and J. Fu, "Impedance Methods for Analyzing Stability Impacts of Inverter-Based Resources: Stability Analysis Tools for Modern Power Systems," in IEEE Electrification Magazine, vol. 9, no. 1, pp. 59, March 2021, doi: 10.1109/MELE.2020.3047166.

[4] M. Cheah-Mane, J. Song, R. Ferrer-San-Jose, E. Prieto-Araujo and O. Gomis-Bellmunt, "Analysis of hybrid LCC-VSC HVDC transmission system configurations," 15th IET International Conference on AC and DC Power Transmission (ACDC 2019), 2019, pp. 1-6, doi: 10.1049/cp.2019.0071.

[5] Grigsby, L.L., "Power System Stability and Control," 3rd Ed, CRC Press, 2012, Ch.8, pp. 3, doi.org/10.4324/b12113

[6] J. Sun, "Small-signal methods for AC distributed power systems– a review," IEEE Trans. Power Electron., Nov. 2009, vol. 24, pp. 2545-2554.

[7] Se-Kyo Chung, "A phase tracking system for three phase utility interface inverters" in IEEE Transactions on Power Electronics, vol.15, no.3, pp.431-438, May 2000

[8] S. Shah, P. Koralewicz, V. Gevorgian, H. Liu and J. Fu, "Impedance Methods for Analyzing Stability Impacts of Inverter-Based Resources: Stability Analysis Tools for Modern Power Systems," in IEEE Electrification Magazine, vol. 9, no. 1, pp. 54-56, March 2021, doi: 10.1109/MELE.2020.3047166.